

HIGH FIDELITY UNIVERSAL SET OF QUANTUM GATES USING NON-ADIABATIC RAPID PASSAGE

RAN LI

*Department of Physics, Kent State University, Stark Campus
North Canton, OH 44720*

MELIQUE HOOVER

*Department of Physics, Southern Illinois University
Carbondale, IL 62901-4401*

FRANK GAITAN^a

*Department of Physics, Southern Illinois University
Carbondale, IL 62901-4401*

Numerical simulation results are presented which suggest that a class of non-adiabatic rapid passage sweeps first realized experimentally in 1991 should be capable of implementing a universal set of quantum gates \mathcal{G}_u that operate with high fidelity. The gates constituting \mathcal{G}_u are the Hadamard and NOT gates, together with variants of the phase, $\pi/8$, and controlled-phase gates. The universality of \mathcal{G}_u is established by showing that it can construct the universal set consisting of Hadamard, phase, $\pi/8$, and controlled-NOT gates. Sweep parameter values are provided which simulations indicate will produce the different gates in \mathcal{G}_u , and for which the gate error probability P_e satisfies: (i) $P_e < 10^{-4}$ for the one-qubit gates; and (ii) $P_e < 1.27 \times 10^{-3}$ for the modified controlled-phase gate. The sweeps in this class are non-composite and generate controllable quantum interference effects that allow the gates in \mathcal{G}_u to operate non-adiabatically while maintaining high fidelity. These interference effects have been observed using NMR, and it has previously been shown how these rapid passage sweeps can be applied to atomic systems using electric fields. Here we show how these sweeps can be applied to both superconducting charge and flux qubit systems. The simulations suggest that the universal set of gates \mathcal{G}_u produced by these rapid passage sweeps shows promise as possible elements of a fault-tolerant scheme for quantum computing.

Keywords: fault-tolerant quantum computation, accuracy threshold, quantum interference, resonance, non-adiabatic dynamics, superconducting qubits

1 Introduction

Slightly more than a decade has passed since the accuracy threshold theorem was first proved, establishing the unexpected result that, under appropriate conditions, a quantum computation

^aCorresponding author.

of arbitrary duration could be carried out with arbitrarily small error probability in the presence of noise, and using imperfect quantum gates [1]–[8]. The required conditions are that: (1) the computational data is protected by a sufficiently layered concatenated quantum error correcting code; (2) fault-tolerant protocols for quantum computation, error correction, and measurement are used; and (3) all quantum gates used in the computation have error probabilities (per operation) P_e that fall below a value known as the accuracy threshold P_a . This threshold has been calculated for a number of simple error models with results falling in the range $10^{-6} < P_a < 10^{-3}$. For many, $P_a \sim 10^{-4}$ has become a rough-and-ready working estimate for the threshold so that gates are anticipated to be approaching the accuracies needed for fault-tolerant quantum computing when $P_e < 10^{-4}$. A number of universal sets of quantum gates have been found [9]–[14]. With such a set of gates, any N -qubit unitary operation can be applied using a quantum circuit made up solely of gates belonging to the universal set. Thus the problem of producing sufficiently accurate quantum gates shifts to producing a sufficiently accurate universal set of such gates. One well-known universal set consists of the one-qubit Hadamard, phase, and $\pi/8$ gates, together with the two-qubit controlled-NOT gate [14].

In this paper numerical simulation results are presented which suggest that a class of non-adiabatic rapid passage sweeps known as twisted rapid passage (TRP), first realized experimentally in 1991 [15], should be capable of implementing a universal set of quantum gates \mathcal{G}_u that operate non-adiabatically and with high fidelity. \mathcal{G}_u consists of the one-qubit Hadamard and NOT gates, together with variants of the: (i) one-qubit phase and $\pi/8$ gates; and (ii) two-qubit controlled-phase gate. The universality of this set is established by showing that it can construct the universal set of Ref. [14]. Sweep parameter values are provided which simulations indicate will produce the different gates in \mathcal{G}_u , and for which the gate error probability P_e satisfies: (i) $P_e < 10^{-4}$ for the one-qubit gates; and (ii) $P_e < 1.27 \times 10^{-3}$ for the modified controlled-phase gate. This level of accuracy is a consequence of controllable quantum interference effects that are generated by this class of rapid passage sweeps [16, 17, 18]. The sweep parameter values provided for each gate were found using an optimization procedure that searches for minima of P_e . TRP implementation of the one-qubit gates in \mathcal{G}_u was shown in Ref. [18]. Here we complete the universal set \mathcal{G}_u by showing that TRP can also implement a high fidelity, non-adiabatic modified controlled-phase gate. TRP sweeps have already been experimentally realized in NMR systems [15, 17]. Ref. [18] showed how TRP sweeps can be applied to atomic systems using electric fields. Here we extend the list of physical systems to which TRP can be applied by showing how these sweeps can be applied to both superconducting charge and flux qubit systems.

The outline of this paper is as follows. Section 2 begins with a summary of the essential properties of TRP. It then details our simulation protocol, and the procedure used to optimize the TRP sweep parameters. Section 3 presents our simulation results for the universal set of gates \mathcal{G}_u . For each gate in \mathcal{G}_u , we present: the optimized sweep parameter values that produce it; an upper bound on the gate error probability P_e ; and the gate fidelity \mathcal{F} . For the two-qubit modified controlled-phase gate, we also include the unitary operation produced. We have not included the corresponding unitary operations for each of the one-qubit gates in \mathcal{G}_u as they appear in Ref. [18]. Section 4 then explains how TRP sweeps can be applied to both superconducting charge and flux qubits. Finally, Section 5 makes closing remarks.

2 Preliminaries

This section discusses a number of important background topics. Section 2.1 provides a brief review of TRP and shows how these sweeps generate quantum interference effects that are controllable through variation of the sweep parameters. Section 2.2 describes the protocol used to simulate the one- and two-qubit gates that are of interest in this paper. Finally, to produce high performance gates, the simulations are combined with an optimization procedure described in Section 2.3 that searches for sweep parameter values that minimize an upper bound on the gate error probability P_e .

2.1 Twisted Rapid Passage

To introduce TRP we consider a single qubit interacting with an external control field $\mathbf{F}(t)$ via the Zeeman interaction

$$H_Z(t) = -\boldsymbol{\sigma} \cdot \mathbf{F}(t), \quad (1)$$

where $\boldsymbol{\sigma}_i$ are the Pauli matrices. The sweeps we will be interested in are a generalization of those used in adiabatic rapid passage (ARP) [19]. In ARP the field $\mathbf{F}(t)$ in the detector frame [20] is inverted over a time T_0 such that $\mathbf{F}(t) = b \hat{\mathbf{x}} + at \hat{\mathbf{z}}$. In the NMR realization of ARP, as seen in the lab frame, the detector frame rotates about the static magnetic field $B_0 \hat{\mathbf{z}}$. In the detector frame, $\hat{\mathbf{z}}$ is chosen parallel to the rotation axis. In the rotating wave approximation the rf-magnetic field \mathbf{B}_{rf} in the lab frame lies in the x - y plane and rotates about the static magnetic field. The detector frame is chosen to rotate with \mathbf{B}_{rf} so that, in this frame, the rf-field is static and its direction defines $\hat{\mathbf{x}}$: $\mathbf{B}_{rf} = b \hat{\mathbf{x}}$. The inversion time T_0 is large compared to the inverse Larmor frequency ω_0^{-1} (viz. adiabatic), though small compared to the thermal relaxation time τ_{th} (viz. rapid). ARP sweeps provide a highly precise method for inverting the Bloch vector $\mathbf{s}_i = \langle \boldsymbol{\sigma}_i \rangle$, although the price paid for this precision is an adiabatic inversion rate. We are interested in a type of rapid passage in which the control field $\mathbf{F}(t)$, as seen in the detector frame, is allowed to twist around in the x - y plane with time-varying azimuthal angle $\phi(t)$, while simultaneously undergoing inversion along the z -axis:

$$\mathbf{F}(t) = b \cos \phi(t) \hat{\mathbf{x}} + b \sin \phi(t) \hat{\mathbf{y}} + at \hat{\mathbf{z}} . \quad (2)$$

Here $-T_0/2 \leq t \leq T_0/2$ and $\hat{\mathbf{y}} = \hat{\mathbf{z}} \times \hat{\mathbf{x}}$. Note that any pair of orthogonal unit vectors in the x - y plane can be used for $\hat{\mathbf{x}}$ and $\hat{\mathbf{y}}$. Different choices simply alter the value of $\phi(t = 0)$. As will be seen shortly, interesting physical effects arise when the twist profile $\phi(t)$ is chosen appropriately. This class of rapid passage sweeps is referred to as twisted rapid passage (TRP). The first experimental realization of TRP in 1991 by Zwanziger et al. [15] carried out the inversion adiabatically with $\phi(t) = Bt^2$. Subsequently, *non-adiabatic* TRP was studied with polynomial twist profile $\phi(t) = (2/n)Bt^n$ [16], and controllable quantum interference effects were found to arise for $n \geq 3$. Zwanziger et al. [17] implemented non-adiabatic polynomial TRP with $n = 3, 4$ and observed the predicted interference effects. In the Zwanziger experiments [15, 17], a TRP sweep is produced by sweeping the detector frequency $\dot{\phi}_{det}(t)$ linearly through resonance at the Larmor frequency ω_0 : $\dot{\phi}_{det}(t) = \omega_0 + (2at)/\hbar$. The frequency of the rf-field $\dot{\phi}_{rf}(t)$ is also swept through resonance in such a way that $\dot{\phi}_{rf}(t) = \dot{\phi}_{det}(t) - \dot{\phi}(t)$, where $\phi(t) = (2/n)Bt^n$ is the TRP polynomial twist profile. Substituting the

expression for $\dot{\phi}_{det}(t)$ into that for $\dot{\phi}_{rf}(t)$ gives

$$\dot{\phi}_{rf}(t) = \omega_0 + \frac{2at}{\hbar} - \dot{\phi}(t) \quad . \quad (3)$$

At resonance $\dot{\phi}_{rf}(t) = \omega_0$. Inserting this condition into eq. (3), it follows that at resonance

$$at - \frac{\hbar}{2}\dot{\phi}(t) = 0 \quad . \quad (4)$$

For polynomial twist $\phi(t) = (2/n)Bt^n$, eq. (4) has $n - 1$ roots, though only real-valued roots correspond to resonance. Ref. [16] showed that for $n \geq 3$, multiple passes through resonance occur during a *single* TRP sweep: (i) for all n when $B > 0$; and (ii) for n odd when $B < 0$. We restrict ourselves to $B > 0$ in the remainder of this paper. In this case, the qubit passes through resonance at the times:

$$t = \begin{cases} 0, (a/\hbar B)^{\frac{1}{n-2}} & (n \text{ odd}) \\ 0, \pm (a/\hbar B)^{\frac{1}{n-2}} & (n \text{ even}) \end{cases} \quad . \quad (5)$$

We see that the time separating the qubit resonances can be altered by variation of the sweep parameters B and a . Ref. [16] showed that these multiple resonances have a strong influence on the qubit transition probability. It was shown that qubit transitions could be significantly enhanced or suppressed by small variation of the sweep parameters, and hence of the time separating the resonances. Plots of the transition probability versus time suggested that the multiple resonances were producing quantum interference effects that could be controlled by variation of the TRP sweep parameters. In Ref. [21] the qubit transition amplitude was calculated to all orders in the non-adiabatic coupling. The result found there can be re-expressed as the following diagrammatic series:

$$T_-(t) = \begin{array}{c} \leftarrow \\ \downarrow \\ \leftarrow \\ \uparrow \\ \leftarrow \end{array} + \begin{array}{c} \leftarrow \\ \downarrow \\ \leftarrow \\ \downarrow \\ \leftarrow \\ \uparrow \\ \leftarrow \\ \downarrow \\ \leftarrow \end{array} + \begin{array}{c} \leftarrow \\ \downarrow \\ \leftarrow \\ \downarrow \\ \leftarrow \\ \uparrow \\ \leftarrow \\ \downarrow \\ \leftarrow \\ \uparrow \\ \leftarrow \\ \downarrow \\ \leftarrow \end{array} + \dots \quad . \quad (6)$$

Lower (upper) lines correspond to propagation in the negative (positive) energy level and the vertical lines correspond to transitions between the two energy levels. The calculation sums the probability amplitudes for all interfering alternatives [22] that allow the qubit to end up in the positive energy level at time t given that it was initially in the negative energy level. As we have seen, varying the TRP sweep parameters varies the time separating the resonances. This in turn changes the value of each diagram in eq. (6), and thus alters the interference between alternatives in the quantum superposition. Similar diagrammatic series can be worked out for the remaining 3 combinations of final and initial states. It is the sensitivity of the individual alternatives/diagrams to the time separation of the resonances that allow TRP to manipulate this quantum interference. Zwanziger et al. [17] observed these interference effects in the transition probability using liquid state NMR and found quantitative agreement between theory and experiment. It is the link between the TRP sweep parameters and this quantum interference that we believe makes it possible for TRP to drive highly accurate non-adiabatic one- and two-qubit gates. The results presented in Section 3 for the different gates in the universal set \mathcal{G}_u are found by numerical simulation of the Schrodinger equation. We next describe how the simulations are done.

2.2 Simulation Protocol

As is well-known, an N -qubit quantum gate applies a fixed unitary transformation U to N -qubit states:

$$|\psi_{out}\rangle = U |\psi_{in}\rangle. \quad (7)$$

We will be interested in the unitary transformations applied by the: (i) one-qubit Hadamard (U_H), phase (U_P), $\pi/8$ ($U_{\pi/8}$), and NOT (U_{NOT}) gates

$$U_H = \frac{1}{\sqrt{2}} \begin{pmatrix} 1 & 1 \\ 1 & -1 \end{pmatrix} \quad ; \quad U_P = \begin{pmatrix} 1 & 0 \\ 0 & i \end{pmatrix} \quad (8)$$

$$U_{\pi/8} = \begin{pmatrix} 1 & 0 \\ 0 & e^{i\pi/4} \end{pmatrix} \quad ; \quad U_{NOT} = \begin{pmatrix} 0 & 1 \\ 1 & 0 \end{pmatrix}, \quad (9)$$

and (ii) the two-qubit controlled-NOT (U_{CNOT}) and controlled-phase (U_{CP}) gates

$$U_{CNOT} = \begin{pmatrix} 1 & 0 & 0 & 0 \\ 0 & 1 & 0 & 0 \\ 0 & 0 & 0 & 1 \\ 0 & 0 & 1 & 0 \end{pmatrix} \quad ; \quad U_{CP} = \begin{pmatrix} 1 & 0 & 0 & 0 \\ 0 & 1 & 0 & 0 \\ 0 & 0 & 1 & 0 \\ 0 & 0 & 0 & -1 \end{pmatrix}. \quad (10)$$

The one- and two-qubit matrices appearing in eqs. (8)–(10) are in the representation spanned by the one- and two-qubit computational basis states $|i\rangle$ and $|ij\rangle$ which are, respectively, the eigenstates of σ_z and $\sigma_z^1 \otimes \sigma_z^2$:

$$\sigma_z |i\rangle = (-1)^i |i\rangle \quad ; \quad \sigma_z^1 \otimes \sigma_z^2 |ij\rangle = (-1)^{i+j} |ij\rangle \quad (i, j = 0, 1). \quad (11)$$

The dynamical impact of TRP is determined by numerical simulation of the Schrodinger equation. Let $H(t)$ denote the Hamiltonian for an N -qubit system, and $|E_k(t)\rangle$ the instantaneous energy eigenstates which satisfy $H(t) |E_k(t)\rangle = E_k(t) |E_k(t)\rangle$ with $k = 1, \dots, 2^N$. It is found that the numerical stability of the simulations is enhanced if we expand $|\psi(t)\rangle$ in the instantaneous energy eigenstates $|E_k(t)\rangle$. Because of the direct connection between these states and $H(t)$, they carry substantial dynamical information, and a substantial portion of the dynamics due to $H(t)$ can be accounted for by choosing this basis. This makes the task of determining the remaining dynamics using the Schrodinger equation much simpler and the simulations more stable. We thus write

$$|\psi(t)\rangle = \sum_{k=1}^{2^N} a_k(t) |E_k(t)\rangle \exp \left[-\frac{i}{\hbar} \int_{-T_0/2}^t d\tau \{ E_k(\tau) - \hbar \dot{\gamma}_k(\tau) \} \right], \quad (12)$$

where $\gamma_k(t)$ is the adiabatic geometric phase [23] associated with the energy level $E_k(t)$, and

$$\dot{\gamma}_k(t) = i \langle E_k(t) | \frac{d}{dt} | E_k(t) \rangle. \quad (13)$$

Substituting eq. (12) into the Schrodinger equation, and using the orthonormality of the instantaneous energy eigenstates, one arrives at the equations of motion for the expansion coefficients $a_k(t)$:

$$\frac{da_k}{dt} = - \sum_{l \neq k} a_l(t) \Gamma_{kl}(t) \exp \left[-i \int_{-T_0/2}^t d\tau \delta_{lk}(\tau) \right], \quad (14)$$

where $k = 1, \dots, 2^N$, and

$$\Gamma_{kl}(t) = \langle E_k(t) | \frac{d}{dt} | E_l(t) \rangle \quad (15)$$

$$\delta_{lk}(t) = \frac{(E_l(t) - E_k(t))}{\hbar} - (\dot{\gamma}_l(t) - \dot{\gamma}_k(t)). \quad (16)$$

The simulations set the initial N -qubit state to be one of the computational basis states $|i_1 \cdots i_{2^N}\rangle$. The simulation outcome is the $|i_1 \cdots i_{2^N}\rangle$ -column of the unitary transformation U produced by the TRP sweep. By simulating all 2^N computational basis states, U is determined column-by-column.

It proves useful to recast eqs. (14) in dimensionless form. For the one-qubit case we introduce the dimensionless time $\tau = (a/b)t$, the dimensionless inversion rate $\lambda = \hbar a/b^2$, and the dimensionless twist strength $\eta_n = (\hbar B/a)(b/a)^{n-2}$. For the remainder of this paper we restrict ourselves to quartic TRP which has twist profile $\phi_n(\tau)$ with $n = 4$:

$$\phi_4(\tau) = \frac{1}{2}B \left(\frac{b\tau}{a} \right)^4 = \left(\frac{\eta_4}{2\lambda} \right) \tau^4. \quad (17)$$

The sweep parameters a , b , and B are chosen to be positive so that λ and η_4 are also positive. The Hamiltonian for the one-qubit gates is the Zeeman Hamiltonian $H_Z(t)$ given in eqs. (1) and (2). The dimensionless version of $H_Z(t)$ is found by multiplying it by $(b/\hbar a)$. Denoting the result by $H_1(\tau)$, one finds

$$H_1(\tau) = -\frac{\tau}{\lambda} \sigma_z - \frac{1}{\lambda} [\cos \phi_4 \sigma_x + \sin \phi_4 \sigma_y], \quad (18)$$

where $\phi_4(\tau)$ is given by eq. (17). $H_1(\tau)$ is the Hamiltonian that drives the one-qubit simulations via eqs. (14)–(16) in dimensionless form.

The derivation of the dimensionless Hamiltonian $H_2(\tau)$ that drives the two-qubit simulations is more complicated and is presented in Appendix A. As explained there, $H_2(\tau)$ includes an interaction that Zeeman-couples each qubit to a TRP control field, as well as an Ising interaction between the two qubits. The Ising interaction was chosen because of its simplicity, and because of its occurrence in many physical systems. Modification of the simulations to include alternative qubit-qubit interactions is straightforward. The resulting two-qubit Hamiltonian yields energy level spacings that give rise to a degeneracy in the resonance energy for the energy level pairs $(E_1 \leftrightarrow E_2)$ and $(E_3 \leftrightarrow E_4)$. To remove this degeneracy the term $\Delta H = c_4 |E_4(t)\rangle \langle E_4(t)|$ is added to the Hamiltonian, where c_4 is a constant. The end result is the Hamiltonian $H_2(\tau)$ that drives the two-qubit simulations:

$$\begin{aligned} H_2(\tau) = & \left[-\frac{(d_1 + d_2)}{2} + \frac{\tau}{\lambda} \right] \sigma_{1z} - \frac{d_3}{\lambda} [\cos \phi_4 \sigma_{1x} + \sin \phi_4 \sigma_{1y}] \\ & + \left[-\frac{d_2}{2} + \frac{\tau}{\lambda} \right] \sigma_{2z} - \frac{1}{\lambda} [\cos \phi_4 \sigma_{2x} + \sin \phi_4 \sigma_{2y}] \\ & - \frac{\pi}{2} d_4 \sigma_{1z} \sigma_{2z} + \Delta H. \end{aligned} \quad (19)$$

The constants d_i ($i = 1, \dots, 4$) are defined in Appendix A where a description of their physical significance is also given.

Having described how the simulations are done, and how we determine the actual unitary transformation U_a produced by a specific assignment of the TRP sweep parameters, we go on in Section 2.3 to explain how the sweep parameters are iteratively modified so as to make U_a approach a target gate U_t as closely as possible.

2.3 Sweep Parameter Optimization

Let \mathcal{H}_N be the Hilbert space for an N -qubit system. As in Section 2.2, let U_a denote the actual unitary operation produced by a given set of TRP sweep parameters, and U_t a target unitary operation we would like TRP to approximate as closely as possible. Introducing the operators $D = U_a - U_t$ and $P = D^\dagger D$, and the normalized state $|\psi\rangle$, we define $|\psi_a\rangle = U_a|\psi\rangle$, $|\psi_t\rangle = U_t|\psi\rangle$, and $|\psi_\perp\rangle = \{I - |\psi_t\rangle\langle\psi_t|\}\psi_a$. Ref. [18] showed that the error probability $P_e(\psi)$ for U_a acting on the state $|\psi\rangle$ is $P_e(\psi) = |\langle\psi_\perp|\psi_\perp\rangle|^2$. The gate error probability P_e for the TRP gate U_a was then defined to be the worst-case error probability:

$$P_e \equiv \max_{|\psi\rangle} P_e(\psi). \quad (20)$$

Because of the search over $|\psi\rangle$, evaluation of P_e from eq. (20) is not practical. Ref. [18] showed that

$$P_e \leq \text{Tr } P, \quad (21)$$

where $P = D^\dagger D$ was defined above. Once U_a has been determined by the numerical simulation, $\text{Tr } P$ is easily calculated, and so it makes a convenient proxy for P_e in the sweep parameter optimization procedure that we are now ready to describe.

To find TRP sweep parameter values that yield highly accurate non-adiabatic quantum gates it proved necessary to combine our simulations with function minimization algorithms [24] that search for sweep parameters that minimize the upper bound $\text{Tr } P$ for the gate error probability P_e . The multi-dimensional downhill simplex method was used for the one-qubit gates in the universal set \mathcal{G}_u , while simulated annealing was used for the two-qubit modified controlled-phase gate. For quartic TRP, the sweep parameters are (λ, η_4) which can be thought of as specifying a point in a two-dimensional parameter space. The downhill simplex method takes as input three sets of sweep parameters which specify the vertices of a simplex in the two-dimensional parameter space. The dynamical effect of the TRP sweep associated with each vertex is found by numerically integrating the Schrodinger equation as described in Section 2.2. The output of the integration is the unitary operation U_a that a particular sweep applies. Having U_a we determine $P = (U_a - U_t)^\dagger (U_a - U_t)$ and evaluate $\text{Tr } P$. The downhill simplex method iteratively alters the simplex (i.e. one or more of its vertices) until sweep parameter values are found that yield a local minimum of $\text{Tr } P$. Because the minimum found is not global, some starting simplexes will give deeper minima than others. Though there was no guarantee, it was hoped that a starting simplex could be found that yielded $\text{Tr } P < 10^{-4}$. Some trial and error in specifying the starting simplex was thus required, though for the one-qubit gates in \mathcal{G}_u , the trial and error procedure eventually proved successful. For the two-qubit modified controlled-phase gate, trial and error proved inadequate, and it was necessary to use simulated annealing to find sweep parameter values that yielded $\text{Tr } P \sim 10^{-3}$. We present our results for all gates in \mathcal{G}_u in the following section.

3 Universal Set of Quantum Gates

To determine fidelities for the TRP gates we use the fidelity

$$\mathcal{F}_n = \frac{1}{2^n} \text{Re} [Tr (U_a^\dagger U_t)], \quad (22)$$

where n denotes the number of qubits acted on by the gate. \mathcal{F}_n is an extension to n qubits of the fidelity used in Ref. [25] for one-qubit gates ($n = 1$). It is possible to relate our $Tr P$ upper bound for P_e to \mathcal{F}_n . Recalling that $P = (U_a - U_t)^\dagger (U_a - U_t)$, it follows that

$$\begin{aligned} Tr P &= Tr \left[2 - (U_a^\dagger U_t + U_t^\dagger U_a) \right] \\ &= 2^{n+1} - 2 \text{Re} [Tr (U_a^\dagger U_t)] \\ &= 2^{n+1} (1 - \mathcal{F}_n), \end{aligned} \quad (23)$$

and so

$$\mathcal{F}_n = 1 - \left(\frac{1}{2^{n+1}} \right) Tr P. \quad (24)$$

$Tr P$ thus yields the fidelity \mathcal{F}_n and an upper bound on the gate error probability P_e .

Next, notice that the gates U_P and $U_{\pi/8}$ (see eqs. (8) and (9)) can be re-written as

$$U_P = e^{i\pi/4} U_{NOT} V_P \quad (25)$$

$$U_{\pi/8} = e^{i\pi/8} U_{NOT} V_{\pi/8}, \quad (26)$$

where

$$V_P = \begin{pmatrix} 0 & e^{i\pi/4} \\ e^{-i\pi/4} & 0 \end{pmatrix} \quad (27)$$

$$V_{\pi/8} = \begin{pmatrix} 0 & e^{i\pi/8} \\ e^{-i\pi/8} & 0 \end{pmatrix}, \quad (28)$$

and U_{NOT} is given in eq. (9). Note also that U_{CNOT} (eq. (10)) can be re-written as

$$U_{CNOT} = (I^1 \otimes U_H^2) [(\sigma_z^1 \otimes I^2) V_{CP}] (I^1 \otimes U_H^2). \quad (29)$$

Here the superscript on a one-qubit gate labels the qubit on which the gate acts, and we have introduced the modified controlled-phase gate

$$V_{CP} = \begin{pmatrix} 1 & 0 & 0 & 0 \\ 0 & 1 & 0 & 0 \\ 0 & 0 & -1 & 0 \\ 0 & 0 & 0 & 1 \end{pmatrix}. \quad (30)$$

Finally, notice that the Pauli matrix σ_z^i can be implemented using the phase gate U_P^i : $\sigma_z^i = (U_P^i)^2$. It follows from this and eqs. (25), (26), and (29) that the set of gates $\{U_H, U_P, U_{\pi/8}, U_{CNOT}\}$ can be constructed using the set $\mathcal{G}_u = \{U_H, U_{NOT}, V_P, V_{\pi/8}, V_{CP}\}$. Since the first set of gates is universal [14], so is the set \mathcal{G}_u . As will be seen below, TRP can be used to produce all gates in \mathcal{G}_u . For each gate we present our best-case result and show how gate performance is altered by small variation of the parameters.

3.1 One-Qubit Gates

A study of the TRP-implementation of the one-qubit gates in \mathcal{G}_u was first reported in Ref. [18]. The essential results are included here for the reader's convenience, though for the sake of brevity, we have not reproduced the unitary operation U_a generated by TRP for each gate. The interested reader can find them displayed in Ref. [18].

As noted in Section 2.2, all results presented in this paper are for quartic TRP which has twist profile

$$\phi(\tau) = \frac{1}{2} \left(\frac{\eta_4}{\lambda} \right) \tau^4. \quad (31)$$

Here τ , λ , and η_4 are dimensionless versions of the time t , inversion rate a , and twist strength B . For the reader's convenience, their definitions (Section 2.1) are restated here:

$$\tau = \left(\frac{a}{b} \right) t \quad ; \quad \lambda = \frac{\hbar a}{b^2} \quad ; \quad \eta_4 = \left(\frac{\hbar b^2}{a^3} \right) B. \quad (32)$$

Throughout this paper we assume a , b , and B are positive. The parameter b was introduced in eq. (2) and is proportional to the rf-field amplitude in an NMR realization of TRP [16, 17]. All simulations were done with $\lambda > 1$ corresponding to non-adiabatic inversion [16, 17], and the dimensionless inversion time $\tau_0 = aT_0/b$ was fixed at 80.000 for the one-qubit simulations, and at 120.00 for the two-qubit simulations.

The translation key connecting the simulation parameters to the experimental sweep parameters used in the (one-qubit) Zwanziger experiments [15, 17] is given in the Appendix of Ref. [16]. We re-write the formulas for quartic twist here for convenience. Note that Zwanziger's symbol B is here replaced by \mathcal{B} to avoid confusion with our use of B to denote the twist strength. First we give the formulas connecting our parameters (a, b, B, T_0) to the Zwanziger parameters ($\omega_1, A, \mathcal{B}, T_0$):

$$\omega_1 = \frac{2b}{\hbar} \quad (33)$$

$$A = \frac{aT_0}{\hbar} \quad (34)$$

$$\mathcal{B} = \frac{BT_0^4}{2}, \quad (35)$$

where the inversion time T_0 is common to both parameter sets. The formulas linking the dimensionless sweep parameters (λ, η_4) to the Zwanziger parameters ($\omega_1, A, \mathcal{B}, T_0$) are:

$$\lambda = \frac{4A}{\omega_1^2 T_0} \quad (36)$$

$$\eta_4 = \frac{\mathcal{B}\omega_1^2}{2A^3 T_0}. \quad (37)$$

In the experiments of Ref. [17]: $\omega_1 = 393$ Hz; $T_0 = 41.00$ ms; $A = 50\,000$ Hz; and \mathcal{B} was calculated from eq. (37) with η_4 varying over the range $[4.50, 4.70] \times 10^{-4}$.

Hadamard Gate

Here the target gate U_t is the Hadamard gate U_H (see eq. (8)). The TRP sweep parameters $\lambda = 5.8511$ and $\eta_4 = 2.9280 \times 10^{-4}$ produce a unitary gate U_a [18] for which $Tr P = 8.82 \times 10^{-6}$.

This yields a gate fidelity $\mathcal{F}_H = 0.9999\ 98$ and the bound $P_e \leq 8.82 \times 10^{-6}$ on the gate error probability. Table 1 shows how gate performance varies when the sweep parameters are altered slightly. Of the two sweep parameters, η_4 is seen to have the largest impact on gate

Table 1. Variation of $Tr P$ for the Hadamard gate when the TRP sweep parameters are altered slightly from their best performance values. The columns to the left of center have $\eta_4 = 2.9280 \times 10^{-4}$ and those to the right have $\lambda = 5.8511$.

η_4	λ	$Tr P$	λ	η_4	$Tr P$
2.9280×10^{-4}	5.8510	7.22×10^{-5}	5.8511	2.9279×10^{-4}	7.03×10^{-4}
	5.8511	8.82×10^{-6}		2.9280×10^{-4}	8.82×10^{-6}
	5.8512	1.84×10^{-5}		2.9281×10^{-4}	6.14×10^{-4}

performance. This will turn out to be true for the other one-qubit gates as well. Although TRP can produce a non-adiabatic Hadamard gate whose error probability falls below the accuracy threshold $P_a \sim 10^{-4}$, it is clear from Table 1 that the sweep parameters must be controlled to 5 significant figures to achieve this level of performance. See Section 5 for further discussion.

V_P Gate

The modified phase gate V_P (see eq. (27)) is the target gate here. The sweep parameters $\lambda = 5.9750$ and $\eta_4 = 3.8060 \times 10^{-4}$ produce a unitary gate U_a [18] which has $Tr P = 8.20 \times 10^{-5}$. This gives a fidelity $\mathcal{F}_{V_P} = 0.9999\ 80$ and the bound $P_e \leq 8.20 \times 10^{-5}$. Table 2 shows how $Tr P$ varies with small changes in λ and η_4 . Again, gate performance is most sensitive to

Table 2. Variation of $Tr P$ for the modified phase gate V_P when the TRP sweep parameters are altered slightly from their best performance values. The columns to the left of center have $\eta_4 = 3.8060 \times 10^{-4}$ and those to the right have $\lambda = 5.9750$.

η_4	λ	$Tr P$	λ	η_4	$Tr P$
3.8060×10^{-4}	5.9749	1.56×10^{-4}	5.9750	3.8059×10^{-4}	2.29×10^{-3}
	5.9750	8.20×10^{-5}		3.8060×10^{-4}	8.20×10^{-5}
	5.9751	1.43×10^{-4}		3.8061×10^{-4}	1.88×10^{-3}

variation of η_4 , and the sweep parameters must be controlled to high precision to surpass the accuracy threshold (see Section 5).

$V_{\pi/8}$ Gate

The target gate this time is the modified $\pi/8$ gate $V_{\pi/8}$ (see eq. (28)). For $\lambda = 6.0150$ and $\eta_4 = 8.1464 \times 10^{-4}$, TRP produces a unitary gate U_a [18] which has $Tr P = 3.03 \times 10^{-5}$, fidelity $\mathcal{F}_{V_{\pi/8}} = 0.9999\ 92$, and $P_e \leq 3.03 \times 10^{-5}$. Table 3 shows how gate performance varies when the sweep parameters are altered slightly. As with the two previous gates, performance is most sensitive to variation of η_4 , and the sweep parameters must be controllable to high precision (see Section 5).

NOT Gate

Here the target gate is the NOT gate (see eq.(9)). For $\lambda = 7.3205$ and $\eta_4 = 2.9277 \times 10^{-4}$, TRP produces the unitary gate U_a [18] for which $Tr P = 1.10 \times 10^{-5}$, fidelity $\mathcal{F}_{NOT} = 0.9999\ 97$,

Table 3. Variation of $Tr P$ for the modified $\pi/8$ gate when the TRP sweep parameters are altered slightly from their best performance values. The columns to the left of center have $\eta_4 = 8.1464 \times 10^{-4}$ and those to the right have $\lambda = 6.0150$.

η_4	λ	$Tr P$	λ	η_4	$Tr P$
8.1464×10^{-4}	6.0149	1.30×10^{-3}	6.0150	8.1463×10^{-4}	1.77×10^{-3}
	6.0150	3.03×10^{-5}		8.1464×10^{-4}	3.03×10^{-5}
	6.0151	2.18×10^{-3}		8.1465×10^{-4}	2.77×10^{-3}

and $P_e \leq 1.10 \times 10^{-5}$. Table 4 shows how small variation of the sweep parameters alters $Tr P$. As with the other one-qubit gates, performance is most sensitive to variation in η_4 , and the

Table 4. Variation of $Tr P$ for the NOT gate when the TRP sweep parameters are altered slightly from their best performance values. The columns to the left of center have $\eta_4 = 2.9277 \times 10^{-4}$ and those to the right have $\lambda = 7.3205$.

η_4	λ	$Tr P$	λ	η_4	$Tr P$
2.9277×10^{-4}	7.3204	1.12×10^{-5}	7.3205	2.9276×10^{-4}	1.23×10^{-3}
	7.3205	1.10×10^{-5}		2.9277×10^{-4}	1.10×10^{-5}
	7.3206	1.22×10^{-5}		2.9278×10^{-4}	1.23×10^{-3}

sweep parameters must be controllable to 5 significant figures for the gate error probability P_e to fall below the accuracy threshold $P_a \sim 10^{-4}$ (see Section 5).

3.2 Modified Controlled-Phase Gate V_{CP}

We complete the TRP implementation of the universal set \mathcal{G}_u by showing how the modified controlled-phase gate V_{CP} can be produced. As shown in Appendix A, the two-qubit Hamiltonian $H_2(\tau)$ used to implement V_{CP} depends on two sets of parameters. The first set (λ, η_4) consists of the now familiar TRP sweep parameters, while the second set $(d_1, d_2, d_3, d_4, c_4)$ consists of parameters such as coupling constants and frequency-related shifts and differences that appear in $H_2(\tau)$. We stress that only the first set are directly related to the TRP sweeps. Unlike the situation encountered in Section 3.1, best gate performance does *not* require high precision control of the TRP sweep parameters λ and η_4 . Instead, the critical parameters for gate performance will turn out to be d_1 , d_4 , and c_4 . As this is the first time we present results for V_{CP} , we also include the unitary gate U_a produced by our best-case choice of parameters.

The target gate V_{CP} has real and imaginary parts (see eq. (30))

$$\begin{aligned}
 Re(V_{CP}) &= \begin{pmatrix} 1 & 0 & 0 & 0 \\ 0 & 1 & 0 & 0 \\ 0 & 0 & -1 & 0 \\ 0 & 0 & 0 & 1 \end{pmatrix} \\
 Im(V_{CP}) &= \begin{pmatrix} 0 & 0 & 0 & 0 \\ 0 & 0 & 0 & 0 \\ 0 & 0 & 0 & 0 \\ 0 & 0 & 0 & 0 \end{pmatrix}.
 \end{aligned} \tag{38}$$

The parameters

$$\begin{aligned} \lambda &= 5.1 & d_1 &= 11.702 & c_4 &= 5.0003 \\ \eta_4 &= 2.4 \times 10^{-4} & d_2 &= -2.6 \\ & & d_3 &= -0.41 \\ & & d_4 &= 6.6650 \end{aligned}$$

produce the gate U_a with

$$\begin{aligned} \text{Re}(U_a) &= \begin{pmatrix} 0.9998 & 0.0155 & 0.0041 & 0.0028 \\ -0.0154 & 0.9997 & -0.0003 & 0.0021 \\ 0.0042 & -0.0002 & -0.9999 & -0.0038 \\ -0.0026 & -0.0021 & -0.0037 & 0.9999 \end{pmatrix} \\ \text{Im}(U_a) &= \begin{pmatrix} 0.0052 & -0.0108 & -0.0031 & -0.0017 \\ -0.0109 & 0.0064 & -0.0084 & 0.0068 \\ 0.0030 & 0.0084 & 0.0060 & -0.0079 \\ -0.0018 & 0.0068 & 0.0079 & 0.0026 \end{pmatrix}. \end{aligned} \quad (39)$$

All two-qubit simulations used a dimensionless inversion time $\tau_0 = 120.00$. From U_a and V_{CP} it follows that $\text{Tr} P = 1.27 \times 10^{-3}$, the gate fidelity $\mathcal{F}_{V_{CP}} = 0.999683$, and $P_e \leq 1.27 \times 10^{-3}$. Table 5 shows how gate performance varies when either λ or η_4 is altered slightly. Notice

Table 5. Variation of $\text{Tr} P$ for the modified controlled-phase gate V_{CP} when the TRP sweep parameters are altered slightly from their best performance values. The columns to the left (right) of center vary λ (η_4), while holding all other parameters fixed.

λ	$\text{Tr} P$	η_4	$\text{Tr} P$
5.0	2.70×10^{-3}	2.3×10^{-4}	1.46×10^{-3}
5.1	1.27×10^{-3}	2.4×10^{-4}	1.27×10^{-3}
5.2	2.10×10^{-3}	2.5×10^{-4}	1.35×10^{-3}

that the TRP sweep parameters only need to be controlled to *two* significant figures. A similar situation occurs for the parameters d_2 and d_3 , though in the interests of brevity, we will not include Tables to show this. Table 6 shows how gate performance varies when either d_1 or d_4 is varied slightly. We see that these parameters need to be controlled to five

Table 6. Variation of $\text{Tr} P$ for the modified controlled-phase gate V_{CP} when the parameters d_1 and d_4 are altered slightly from their best performance values. The columns to the left (right) of center vary d_1 (d_4), while holding all other parameters fixed.

d_1	$\text{Tr} P$	d_4	$\text{Tr} P$
11.699	1.41×10^{-2}	6.6647	1.31×10^{-2}
11.700	7.63×10^{-3}	6.6648	6.35×10^{-3}
11.701	3.36×10^{-3}	6.6649	2.40×10^{-3}
11.702	1.27×10^{-3}	6.6650	1.27×10^{-3}
11.703	1.43×10^{-3}	6.6651	2.97×10^{-3}
11.704	3.79×10^{-3}	6.6652	7.59×10^{-3}
11.705	8.27×10^{-3}	6.6653	1.50×10^{-2}

significant figures, although a small amount of uncertainty in the fifth significant figure will not drastically damage performance. Recall from Appendix A that d_1 is the dimensionless

version of the difference in qubit Larmor frequencies, and d_4 is the dimensionless Ising coupling constant. Finally, Table 7 shows how TrP varies when c_4 changes slightly. We see that best

Table 7. Variation of TrP for the modified controlled-phase gate V_{CP} when the parameter c_4 is varied slightly from its best performance value. The columns to the left (right) of center vary c_4 in the fifth (fourth) significant figure, while holding all other parameters fixed.

c_4	TrP	c_4	TrP
5.0000	1.98×10^{-3}	4.999	1.50×10^{-2}
5.0001	1.55×10^{-3}	5.000	1.98×10^{-3}
5.0002	1.36×10^{-3}	5.001	5.48×10^{-3}
5.0003	1.27×10^{-3}		
5.0004	1.38×10^{-3}		
5.0005	1.65×10^{-3}		
5.0006	2.11×10^{-3}		

performance is not seriously compromised if c_4 has a small uncertainty in its fifth significant figure. Interestingly, if c_4 can be controlled to four significant figures, we can come very close to best performance. As shown in Appendix A, c_4 is a dimensionless degeneracy-breaking parameter. Although gate performance for V_{CP} is slightly more robust than for the one-qubit gates of Section 3.1, we have not yet been able to find a combination of sweep parameters and two-qubit interaction that yields $P_e < 10^{-4}$. See Section 5 for further discussion.

4 Realizing TRP in Superconducting Qubit Systems

Here we demonstrate how TRP sweeps can be applied to superconducting (SC) qubit systems [26, 27]. We first consider a SC charge qubit in Section 4.1, then go on to flux qubits in Section 4.2. Two realizations of a flux qubit are considered: first the rf-SQUID qubit in Section 4.2.1, then the persistent-current qubit in Section 4.2.2. For each of these qubit realizations, the demonstration proceeds in 3 steps: (i) the appropriate one-qubit Hamiltonian is introduced; (ii) the coefficients of σ_z and σ_x in this Hamiltonian are identified with at and $b \cos \phi_{trp}(t)$, respectively; and (iii) the rotating-wave approximation is invoked to obtain the one-qubit TRP Hamiltonian (see eqs. (1) and (2)). In each demonstration, the second step establishes the link between the theoretical parameters $(a, b, \phi_{trp}(t))$ and the experimental control fields acting on the SC qubit.

4.1 Superconducting Charge Qubit

Figure 1 shows a quantum circuit that can act as a charge qubit with adjustable Josephson coupling [28, 29, 30]. The circuit consists of a superconducting (SC) island that is connected to a SC electrode via a dc-SQUID that is threaded by an external magnetic flux Φ_x , as well as to a gate voltage V_g through a capacitor C_g . The dc-SQUID is designed to have low self-inductance and is made up of two identical Josephson junctions (JJ), each with Josephson coupling energy E_J^0 and capacitance C_J . The SC energy gap Δ is assumed to be the largest energy scale for the circuit dynamics so that at sufficiently low temperature only Cooper pairs can tunnel through the JJs. Denoting the number operator for Cooper pairs on the island by \hat{n} and the phase of the SC order parameter by θ , the Hamiltonian for the SC island is

$$H = 4E_c (\hat{n} - n_g)^2 - E_J(\Phi_x) \cos \theta. \quad (40)$$

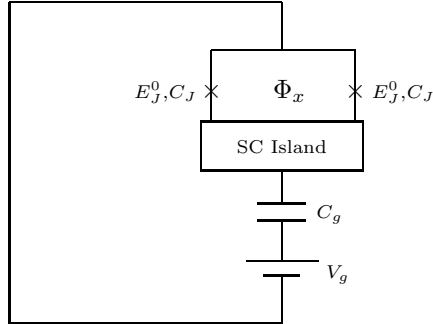


Fig. 1. Quantum circuit for a charge qubit with tunable Josephson coupling. The superconducting (SC) island is connected to a SC electrode through a dc-SQUID that is threaded by an external magnetic flux Φ_x . Each cross \times in the dc-SQUID represents a Josephson junction. The island is also coupled to a gate voltage V_g through a capacitor C_g .

Here: (i) $n_g = C_g V_g / 2e$; (ii) $E_c \equiv 0.5e^2 / (C_g + 2C_J)$ is the charging energy; and (iii) the flux-controlled Josephson coupling energy is $E_J(\Phi_x) = 2E_J^0 \cos(\pi\Phi_x/\Phi_0)$, where $\Phi_0 = h/2e$ is the flux quantum. The number operator \hat{n} and the phase θ are canonically conjugate variables subject to the uncertainty relation $\Delta n \Delta \theta \geq 1$ [31]. In the charging limit ($E_c \gg E_J^0$) H is dominated by the charging term in eq. (40). In this case the eigenstates $|n\rangle$ of \hat{n} form a convenient basis with which to represent H . Because of Cooper pair tunneling, the Josephson coupling term in H will have matrix elements connecting the states $|n\rangle \leftrightarrow |n+1\rangle$. It follows from these remarks that H can be written as

$$H = \sum_n \left\{ 4E_c (n - n_g)^2 |n\rangle\langle n| - \frac{E_J(\Phi_x)}{2} [|n\rangle\langle n+1| + |n+1\rangle\langle n|] \right\}. \quad (41)$$

Note that in the absence of the Josephson coupling term, and for $n_g = 1/2$, the states $|0\rangle$ and $|1\rangle$ have degenerate energies: $E_0 = E_1 = E_c$. In fact, a level-crossing occurs at this value of n_g . The presence of the Josephson coupling in H causes an avoided crossing to occur at $n_g = 1/2$, opening an energy gap $\Delta E_{01} = E_J(\Phi_x) \ll E_c$. Near the degeneracy point ($n_g = 1/2$), these two states have the smallest energy eigenvalues. Thus at low temperature, and for low frequency gate voltage $V_g(t)$ and external magnetic flux $\Phi_x(t)$, the circuit dynamics near the degeneracy point is restricted to the subspace spanned by the states $|0\rangle$ and $|1\rangle$. Under these conditions, the only terms in H that are dynamically relevant are those that act on this subspace. Truncating H so that only those terms are kept gives the SC charge qubit Hamiltonian

$$H_{cq} = -\frac{1}{2} \boldsymbol{\sigma} \cdot \mathbf{B}, \quad (42)$$

where

$$\begin{aligned} B_z &= 4E_c (1 - 2n_g) \\ B_x &= E_J(\Phi_x) \\ B_y &= 0. \end{aligned} \quad (43)$$

This completes the first step of the demonstration.

To apply a TRP sweep to a charge qubit we must require that

$$\begin{aligned}\frac{B_z}{2} &= at \\ \frac{B_x}{2} &= b \cos \phi_{trp},\end{aligned}\tag{44}$$

where $\phi_{trp} = (2/n) Bt^n$ is the TRP twist profile. This is step 2 in the demonstration. With these assignments, eq. (42) becomes

$$H_{cq} = -at \sigma_z - b \cos \phi_{trp} \sigma_x.\tag{45}$$

In the rotating wave approximation (step 3) this becomes

$$H_{cq} = -at \sigma_z - b \cos \phi_{trp} \sigma_x - b \sin \phi_{trp} \sigma_y.\tag{46}$$

Comparing this with eqs. (1) and (2), we see that eq. (46) is the Hamiltonian for a qubit interacting with a TRP sweep. Plugging eqs. (43) into eqs. (44), and recalling that $E_J(\Phi_x) = 2E_J^0 \cos(\pi\Phi_x/\Phi_0)$ gives

$$V_g(t) = \frac{e}{C_g} \left(1 - \frac{at}{2E_c} \right)\tag{47}$$

$$\Phi_x(t) = \left(\frac{\Phi_0}{\pi} \right) \phi_{trp}(t)\tag{48}$$

$$E_J^0 = b.\tag{49}$$

Eqs. (47) and (48) specify the time dependence that $V_g(t)$ and $\Phi_x(t)$ must have, respectively, for a TRP sweep to be applied to a SC charge qubit, and eq. (49) links the sweep parameter b to the Josephson coupling energy E_J^0 . The TRP sweep parameters a , B , and T_0 can then be found from eq. (32) for given values of λ , η_4 , and τ_0 . Varying the gate voltage $V_g(t)$ according to eq. (47) produces the inversion of the TRP control field $\mathbf{F}(t)$ in eq. (2), while varying the flux $\Phi_x(t)$ through the dc-SQUID according to eq. (48), together with eq. (49) and the rotating-wave approximation, produces its twisting in the x - y plane.

4.2 Superconducting Flux Qubit

We examine two flux qubit proposals: (i) the rf-SQUID qubit (Section 4.2.1); and (ii) the persistent-current qubit (Section 4.2.2).

4.2.1 rf-SQUID Qubit

In an rf-SQUID a single Josephson junction (JJ) interrupts a superconducting (SC) loop that is threaded by an external magnetic flux Φ_x . Because the loop has non-vanishing self-inductance L , a secondary flux $\Phi_s = Li_s$ is present whenever a supercurrent i_s circulates around the loop. The total flux $\Phi = \Phi_x + \Phi_s$ determines: (i) the phase difference φ across the JJ via $\varphi = 2\pi \Phi/\Phi_0 \pmod{2\pi}$; and (ii) the supercurrent i_s via $i_s = i_c \sin(2\pi\Phi/\Phi_0)$. Here i_c is the critical current for the junction, and $\Phi_0 = h/2e$ is the flux quantum. The potential

energy for the rf-SQUID is the sum of the Josephson coupling energy and the magnetic energy associated with the secondary flux $\Phi_s = \Phi - \Phi_x$:

$$U(\Phi) = -E_J^0 \cos\left(2\pi \frac{\Phi}{\Phi_0}\right) + \frac{(\Phi - \Phi_x)^2}{2L}; \quad (50)$$

here E_J^0 is the coupling energy. $U(\Phi)$ has a number of important properties. First, $U(\Phi)$ forms a double-well potential for Φ -values near $\Phi_0/2$ when: (i) $\Phi_x \approx \Phi_0/2$; and (ii) the self-inductance L is large enough to cause $\beta_L = E_J^0/(\Phi_0^2/4\pi^2 L) > 1$. The minima occur at $\Phi_{\pm} = \Phi_0/2 \pm \delta\Phi_{\pm}$, and the supercurrents corresponding to these minima, $i_{\pm} = \mp i_c \sin(2\pi\delta\Phi_{\pm}/\Phi_0)$, have opposite circulations. When $\Phi_x = \Phi_0/2$, the double-well potential is symmetric; the central barrier has a maximum at $\Phi = \Phi_0/2$, and the barrier height at maximum is E_J^0 . When $\Phi_x = \Phi_0/2 + \delta\Phi_x$, the double-well potential is asymmetric, and for small $\delta\Phi_x$, the barrier height at maximum remains of order E_J^0 .

The quantum degree of freedom for an rf-SQUID is the total flux Φ , or equivalently, the supercurrent i_s . In the absence of tunneling through the central barrier, the groundstate is doubly degenerate and the energy eigenstates $|L\rangle$ and $|R\rangle$ are localized, respectively, about the left and right minima of the double-well potential. Tunneling splits the degeneracy and the new energy eigenstates $|E_s\rangle$ and $|E_a\rangle$ are, respectively, symmetric and antisymmetric linear combinations of $|L\rangle$ and $|R\rangle$. At sufficiently low temperature the rf-SQUID is limited to the subspace of states spanned by $|E_s\rangle$ and $|E_a\rangle$. Bocko et al. [32] were the first to propose using a low-temperature rf-SQUID as a qubit. The computational basis states (CBS) $|0\rangle$ and $|1\rangle$ are identified with the states $|R\rangle$ and $|L\rangle$, respectively, and are defined to be eigenstates of the operator σ_z : $\sigma_z|i\rangle = (-1)^i|i\rangle$ with $i = 0, 1$. For $\Phi_x \approx \Phi_0/2$, the asymmetry of the double-well potential introduces a bias ϵ in the minima of the double-well:

$$\epsilon = U(\Phi_-) - U(\Phi_+) = 4\pi E_J^0 \sqrt{6(\beta_L - 1)} \left(\frac{\Phi_x}{\Phi_0} - \frac{1}{2} \right). \quad (51)$$

In the absence of tunneling, the energy E_0 (E_1) of the state $|R\rangle = |0\rangle$ ($|L\rangle = |1\rangle$) is well approximated by the sum of $U(\Phi_+)$ ($U(\Phi_-)$) and the groundstate energy of a harmonic oscillator with frequency determined by the double-well curvature at $\Phi = \Phi_+$ ($\Phi = \Phi_-$). For small asymmetry, the energy difference $E_1 - E_0$ for the CBS is then ϵ . To account for this, the flux qubit Hamiltonian H_{f1} includes the term $-(\epsilon/2)\sigma_z$, where the zero of energy has been set at $(E_0 + E_1)/2$. Note that this term in H_{f1} can be varied by varying the flux Φ_x which alters the asymmetry of the double-well, and thus the bias ϵ . Tunneling between wells causes a bit-flip operation $|0\rangle \leftrightarrow |1\rangle$ to be applied to the qubit state. If $(\beta_L - 1) \ll 1$, eq. (51) indicates that $|\epsilon| \ll E_J^0$, and so the energies $\mp\epsilon/2$ of the two lowest energy eigenstates are well below the barrier maximum. WKB theory can thus be used to determine the amplitude $t_{lr}/2$ for the qubit to tunnel from the left to the right well (the factor of 1/2 is introduced for convenience). On the basis of the above remarks, we are led to the flux qubit Hamiltonian

$$H_{f1} = -\frac{\epsilon}{2} \sigma_z - \frac{t_{lr}}{2} \sigma_x = -\frac{1}{2} \boldsymbol{\sigma} \cdot \mathbf{B}, \quad (52)$$

where

$$\begin{aligned} B_z &= \epsilon \\ B_x &= t_{lr} \\ B_y &= 0. \end{aligned} \tag{53}$$

The tunneling amplitude $t_{lr}/2$ is highly sensitive to the barrier height which, as noted earlier, is of order E_J^0 . If the JJ in the rf-SQUID is replaced by a dc-SQUID threaded by an external flux $\tilde{\Phi}_x$ (as in Section 4.1), the coupling energy becomes adjustable, $E_J^0 \rightarrow E_J(\tilde{\Phi}_x) = 2E_J^0 \cos(\pi\tilde{\Phi}_x/\Phi_0)$, and $\tilde{\Phi}_x$ can be used to vary $B_x = t_{lr}$. With this modification, both terms in H_{f1} are experimentally controllable. This leads us to the quantum circuit in Figure 2 for an rf-SQUID flux qubit. The JJs in the dc-SQUID are identical and have coupling energy E_J^0

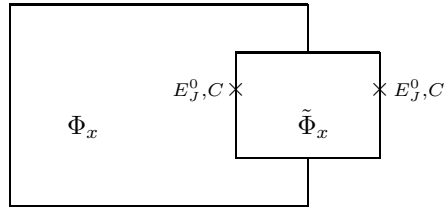


Fig. 2. Quantum circuit for an rf-SQUID flux qubit with tunable Josephson coupling. The larger superconducting loop is threaded by an external magnetic flux Φ_x , while the smaller loop in the dc-SQUID is threaded by the external flux $\tilde{\Phi}_x$. Each cross \times in the dc-SQUID represents a Josephson junction with coupling energy E_J^0 and capacitance C .

and capacitance C . The WKB expression for $t_{lr}/2$ is [33]

$$\frac{t_{lr}}{2} = \frac{\hbar\omega_*}{2\pi} \exp \left[-\frac{1}{\hbar} \int_{\Phi_-}^{\Phi_+} df \sqrt{2M_{nn}|E - U|} \right]. \tag{54}$$

Here ω_* is the attempt frequency; $f = 2\pi [(\Phi/\Phi_0) - (1/2)]$; $M_{nn} = 2C$; and E is the energy. Following Ref. [33] we find that

$$\omega_* = \sqrt{\frac{\beta_L - 1}{LC}}, \tag{55}$$

and denoting the argument of the exponential in eq. (54) by I , we find that

$$I = \frac{8\sqrt{LC}}{\hbar} (\beta_L - 1)^{3/2} E_J(\tilde{\Phi}_x). \tag{56}$$

Eqs. (52)–(56) complete the first step of our demonstration.

To produce a TRP sweep the time-dependence of Φ_x and $\tilde{\Phi}_x$ must be such that

$$at = \frac{B_z}{2} \tag{57}$$

$$b \cos \phi_{trp} = \frac{B_x}{2}. \tag{58}$$

In principle, this completes step 2 of the demonstration. In actuality, a bit more work is needed to fully establish the link between the theory parameters and the control fluxes appearing in Figure 2. To that end, substituting for B_z using eqs. (51) and (53) in eq. (57) gives

$$at = 2\pi \left\{ \frac{\Phi_x}{\Phi_0} - \frac{1}{2} \right\} \left[E_J(\tilde{\Phi}_x) \sqrt{6(\beta_L - 1)} \right], \quad (59)$$

where $E_J^0 \rightarrow E_J(\tilde{\Phi}_x)$ due to the dc-SQUID in Figure 2, and $\beta_L = E_J(\tilde{\Phi}_x) / (\Phi_0^2 / 4\pi^2 L)$. It will be seen below that eq. (58) requires $\tilde{\Phi}_x$ to be time-dependent, and yet we would like the term in the square bracket in eq. (59) to be constant. To achieve this we write

$$\tilde{\Phi}_x = \tilde{\Phi}_x^0 + \delta\tilde{\Phi}_x, \quad (60)$$

where $\tilde{\Phi}_x^0$ is time-independent and will be specified below, and we require that $\pi\delta\tilde{\Phi}_x/\Phi_0 \ll 1$. Then we can write

$$E_J(\tilde{\Phi}_x) = E_J(\tilde{\Phi}_x^0) + \delta E_J \quad (61)$$

and

$$\beta_L = \beta_L^0 + \delta\beta_L, \quad (62)$$

where

$$E_J(\tilde{\Phi}_x^0) = 2E_J^0 \cos\left(\frac{\pi\tilde{\Phi}_x^0}{\Phi_0}\right) \quad ; \quad \delta E_J = -E_J(\tilde{\Phi}_x^0) \tan\left(\frac{\pi\tilde{\Phi}_x^0}{\Phi_0}\right) \left(\frac{\pi\delta\tilde{\Phi}_x}{\Phi_0}\right) \quad (63)$$

and

$$\beta_L^0 = \frac{E_J(\tilde{\Phi}_x^0)}{\left(\frac{\Phi_0^2}{4\pi^2 L}\right)} \quad ; \quad \delta\beta_L = \frac{\delta E_J}{\left(\frac{\Phi_0^2}{4\pi^2 L}\right)}. \quad (64)$$

We now require that $|\delta E_J| \ll E_J(\tilde{\Phi}_x^0)$ and $\delta\beta_L \ll \beta_L^0 - 1$ so that eq. (59) can be written as

$$at = 2\pi \left\{ \frac{\Phi_x}{\Phi_0} - \frac{1}{2} \right\} \left[E_J(\tilde{\Phi}_x^0) \sqrt{6(\beta_L^0 - 1)} \right]. \quad (65)$$

Solving for $\Phi_x(t)$ gives

$$\Phi_x(t) = \frac{\Phi_0}{2} \left[1 + \frac{at}{\pi E_J(\tilde{\Phi}_x^0) \sqrt{6(\beta_L^0 - 1)}} \right]. \quad (66)$$

By requiring that the flux $\Phi_x(t)$ satisfy eq. (66), we insure that the σ_z term in H_{f1} has the appropriate at coefficient needed for a TRP sweep. Thus appropriate variation of the flux $\Phi_x(t)$ through the primary loop in Figure 2 produces the inversion of the z-component of the control field $\mathbf{F}(t)$ in eq. (2). Next we use eq. (58) to determine the flux $\tilde{\Phi}_x(t)$ through the dc-SQUID in Figure 2. Using eqs. (53)–(56) in eq. (58) gives

$$b \cos \phi_{trp} = \frac{\hbar}{2\pi} \omega_* e^{-I}. \quad (67)$$

Writing $I = I_0 + \delta I$, where $\delta I \ll I$ and

$$I_0 = \frac{8\sqrt{LC}}{\hbar} (\beta_L^0 - 1)^{3/2} E_J(\tilde{\Phi}_x^0) \quad (68)$$

$$\delta I = I_0 \left[\frac{3}{2} \frac{\delta\beta_L}{(\beta_L^0 - 1)} + \frac{\delta E_J}{E_J(\tilde{\Phi}_x^0)} \right], \quad (69)$$

allows eq. (67) to be written as

$$b \cos \phi_{trp} = \frac{\hbar}{2\pi} \omega_*^0 e^{-I_0} \left[1 - I_0 \left(\frac{3}{2} \frac{\delta\beta_L}{(\beta_L^0 - 1)} + \frac{\delta E_J}{E_J(\tilde{\Phi}_x^0)} \right) \right]. \quad (70)$$

Note that $\omega_* = \omega_*^0 + \delta\omega_*$ has been written as ω_*^0 in eq. (70), where

$$\omega_*^0 = \sqrt{\frac{\beta_L^0 - 1}{LC}}. \quad (71)$$

The reason for this is that the δI contribution to eq. (70) dominates the $\delta\omega_*$ contribution, and so the latter contribution can be safely discarded. Using eqs. (63) and (64) in eq. (70), along with some algebra, gives

$$(b \cos \phi_{trp}) \left[\frac{2\pi}{\hbar\omega_*^0} e^{I_0} \right] = 1 - \frac{I_0}{2} \frac{(5\beta_L^0 - 2)}{(\beta_L^0 - 1)} \frac{\delta E_J}{E_J(\tilde{\Phi}_x^0)}. \quad (72)$$

Finally, using eq. (63) again, and solving for $\pi\delta\tilde{\Phi}_x/\Phi_0$ gives

$$\frac{\pi\delta\tilde{\Phi}_x}{\Phi_0} = C \cos \phi_{trp} - D, \quad (73)$$

where

$$C = \frac{1}{8\sqrt{LC}} \left(\frac{b}{\hbar} \right) \left(\frac{\hbar}{E_J^0} \right) \left(\frac{2\pi}{\omega_*^0} \right) \left[\frac{\csc \frac{\pi\tilde{\Phi}_x^0}{\Phi_0}}{(5\beta_L^0 - 2)\sqrt{\beta_L^0 - 1}} \right] \exp [I_0]$$

$$D = \left(\frac{1}{8\sqrt{LC}} \right) \left(\frac{\csc \frac{\pi\tilde{\Phi}_x^0}{\Phi_0}}{(5\beta_L^0 - 2)\sqrt{\beta_L^0 - 1}} \right) \left(\frac{\hbar}{E_J^0} \right). \quad (74)$$

Typical values for the parameters in eqs. (74) are: $\beta_L^0 - 1 = 0.1$; $\sqrt{LC} = 1$ ns; and $E_J^0/\hbar = 100$ GHz. With these values, and choosing $b/\hbar = 400$ Hz, and

$$\tilde{\Phi}_x^0/\Phi_0 = 1/2 - \epsilon/\pi, \quad (75)$$

with $\epsilon = 0.25$ gives

$$\omega_*^0 = 0.32 \text{ GHz}$$

$$I_0 = 12.7.$$

From these values we find that

$$\begin{aligned} C &= 2.9 \times 10^{-3} \\ D &= 1.1 \times 10^{-3}, \end{aligned}$$

and from eq. (73), it follows that $\pi\delta\tilde{\Phi}_x/\Phi_0 \approx 10^{-3} \ll 1$ as required. The TRP sweep parameters a , B , and T_0 are then determined from eq. (32) for given values of λ , η_4 , and τ_0 . Thus, with Φ_x given by eq. (66) and $\tilde{\Phi}_x$ given by eqs. (60), (73), and (75), we arrive at the flux qubit Hamiltonian is

$$H_{f1} = -at\sigma_z - b \cos \phi_{trp} \sigma_x.$$

We see that $\Phi_x(t)$ produces the inversion in the TRP control field $\mathbf{F}(t)$ in eq. (2), while $\tilde{\Phi}_x(t)$ will be seen momentarily to give rise to its twisting in the x - y plane. This finally completes step 2. In the rotating wave approximation (step 3), H_{f1} becomes

$$H_{f1} = -at\sigma_z - b \cos \phi_{trp} \sigma_x - b \sin \phi_{trp} \sigma_y, \quad (76)$$

which is the Hamiltonian for a qubit acted on by a TRP sweep (eqs. (1) and (2)).

4.2.2 Persistent-Current Qubit

The focus here is the 4-junction persistent-current qubit introduced in Refs. [33, 34, 35]. The quantum circuit for this qubit is shown in Figure 3. It consists of a loop with negligible

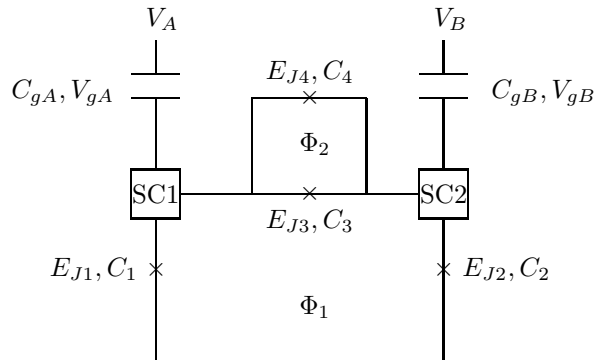


Fig. 3. Quantum circuit for a 4-Josephson junction persistent-current qubit. Junctions 1 and 2 are identical and have coupling energy $E_{J1} = E_{J2} = E_J^0$ and capacitance $C_1 = C_2 = C$. Junctions 3 and 4 are also identical, with coupling energy $E_{J3} = E_{J4} = \beta E_J^0$ and capacitance $C_3 = C_4 = \beta C$. Superconducting islands SC1 and SC2 are, respectively, connected to gate voltages V_A and V_B through gate capacitors C_{gA} and C_{gB} , where $C_{gA} = C_{gB} = \gamma C$. The potential difference across each gate capacitor is V_{gI} , where $I = A, B$. Finally, the dc-SQUID loop is threaded by a flux Φ_2 , while the lower loop is threaded by a flux Φ_1 .

self-inductance that is threaded by an external magnetic flux Φ_1 . Because of the small self-inductance, a supercurrent i_s circulating around the loop produces negligible secondary flux and so the total flux through the loop Φ is given by the external flux Φ_1 . The loop is interrupted by two identical Josephson junctions 1 and 2; a dc-SQUID containing two identical junctions 3 and 4 whose loop is threaded by a flux Φ_2 ; and two superconducting islands SC1 and SC2. Junctions 1 and 2 both have coupling energy E_J^0 and capacitance C , while

junctions 3 and 4 have coupling energy βE_J^0 and capacitance βC . Superconducting island SC1 (SC2) is connected to a gate voltage V_A (V_B) through a gate capacitor C_{gA} (C_{gB}). The gate capacitors are identical with $C_{gA} = C_{gB} = \gamma C$, and capacitor C_{gI} has a potential difference V_{gI} across it, where $I = A, B$. The circuit is assumed to be at sufficiently low temperature that only supercurrents flow in it.

It is conventional to introduce the magnetic frustration $f_i = \Phi_i/\Phi_0$, where $\Phi_0 = h/2e$ is the flux quantum and $i = 1, 2$. Denoting the Josephson phase difference across the j^{th} junction by φ_j , fluxoid quantization around the dc-SQUID loop in Figure 3 requires $\varphi_4 - \varphi_3 = -2\pi f_2$, and around the lower loop requires $\varphi_1 - \varphi_2 + \varphi_3 = -2\pi f_1$. Adding up the Josephson coupling energy for each junction and using the fluxoid quantization relations gives the total Josephson energy U :

$$\frac{U}{E_J^0} = 2 + 2\beta - 2 \cos \varphi_p \cos \varphi_m - \{2\beta \cos(\pi f_a)\} \cos(2\pi f_b + 2\varphi_m), \quad (77)$$

where $\varphi_p = (\varphi_1 + \varphi_2)/2$; $\varphi_m = (\varphi_1 - \varphi_2)/2$; $f_a = f_2$; and $f_b = f_1 + (f_2/2)$. The Josephson energy U acts as the potential energy for the persistent-current qubit. It is periodic in f_b with period 1, and is symmetric about $f_b = 1/2$. At the degeneracy point $f_b = 1/2$, $\alpha = 2\beta \cos(\pi f_a) = 1/2$, U has degenerate minima at $(\varphi_p, \varphi_m) = (0, \pm\varphi_m^*)$, where $\cos \varphi_m^* = 1/(2\alpha)$. Because U is periodic in φ_p and φ_m , the degenerate minima trace out a lattice whose primitive unit cell contains only one pair of degenerate minima. When f_b is near $1/2$, the pair of minima inside a unit cell are no longer degenerate. Within a unit cell, the potential U takes the form of a double well potential which is symmetric when $f_b = 1/2$, and is asymmetric when f_b is near $1/2$. Variation of α allows the potential energy landscape to be further modified. In particular, α can be used to suppress tunneling between minima located in different unit cells.

In the quantum limit: (i) the fluxes φ_p and φ_m become quantum degrees of freedom with conjugate momenta $P_p = -i\hbar\partial/\partial\varphi_p$ and $P_m = -i\hbar\partial/\partial\varphi_m$; and (ii) the Hamiltonian driving the quantum dynamics is

$$H = \frac{P_p^2}{2M_p} + \frac{P_m^2}{2M_m} + E_J^0 U.$$

Here $M_p = (\Phi_0/2\pi)^2 (1 + \gamma) (2C)$ and $M_m = (\Phi_0/2\pi)^2 (1 + 4\beta + \gamma) (2C)$. The energy levels form bands due to the periodicity of U , and the bands are symmetric about $f_b = 1/2$. At sufficiently low temperature, and for f_b near $1/2$, the circuit is effectively restricted to the subspace spanned by the two lowest energy eigenstates $|E_0\rangle$ and $|E_1\rangle$. Persistent supercurrents i_0 and i_1 flow in $|E_0\rangle$ and $|E_1\rangle$, respectively, and $i_0 = -i_1$. These two eigenstates constitute the CBS $|0\rangle$ and $|1\rangle$, and the bit values are encoded into the direction of circulation of the persistent-currents. In the tight-binding approximation the states $|E_0\rangle$ and $|E_1\rangle$ are localized near the minima of U , and (as noted earlier) within a unit cell, U has the form of a double well potential. Focusing on the unit cell containing the minima $(0, \pm\varphi_m^*)$, and denoting the state localized about the minimum $(0, +\varphi_m^*)$ ($(0, -\varphi_m^*)$) by $|+\rangle$ ($|-\rangle$), inside this unit cell we have $|E_0\rangle = [|+\rangle + |-\rangle]/\sqrt{2}$ and $|E_1\rangle = [|+\rangle - |-\rangle]/\sqrt{2}$. When $\alpha = 2\beta \cos(\pi f_a)$ is chosen appropriately, tunneling can be restricted to the two minima within a unit cell. In the absence of tunneling, $|+\rangle$ ($|-\rangle$) is the groundstate of a qubit localized in the well centered about $(0, +\varphi_m^*)$ ($(0, -\varphi_m^*)$). Altering f_b alters the energies E_{\pm} of the states $|\pm\rangle$, and so alters the bias $F = (E_+ - E_-)/2$. Altering f_a alters the barrier height, and so alters the

tunneling amplitude t . Thus, in the representation spanned by $|\pm\rangle$, the persistent-current qubit Hamiltonian H_{f_2} is

$$H_{f_2} = \begin{pmatrix} -F & -t \\ -t & F \end{pmatrix}.$$

Since the CBS are the eigenstates of H_{f_2} , we can also write

$$H_{f_2} = -\sqrt{F^2 + t^2} \sigma_z,$$

where $\sigma_z = |0\rangle\langle 0| - |1\rangle\langle 1|$. Following Ref. [33], the quantum circuit is to operate near the degeneracy point at which $f_1^* = f_2^* = 1/3$. The operating point is chosen to have $f_1^o = f_1^* + \epsilon_1$ and $f_2^o = f_2^* + \epsilon_2$. It can be shown that, at the operating point, the bias is $F_o = r_1\epsilon_1 + r_2\epsilon_2$ and the tunneling amplitude is $t_o = t_* + s_2\epsilon_2$, where t_* is the tunneling amplitude at the degeneracy point. Explicit formulas for r_1 , r_2 , and s_2 appear in Ref. [33], though they will not be needed here. By varying $f_1 = f_1^o + \delta_1$ and $f_2 = f_2^o + \delta_2$ about the operating point with time-dependent δ_1 and δ_2 , a unitary transformation can be applied to the qubit. Defining $\tan \theta_o = -t_o/F_o$, the Hamiltonian H_{f_2} becomes

$$H_{f_2} = [-Z_0 + Z_1 \delta_1 + Z_2 \delta_2] \sigma_z - [X_1 \delta_1 + X_2 \delta_2] \sigma_x, \quad (78)$$

where

$$\begin{aligned} Z_0 &= \sqrt{F_o^2 + t_o^2} \\ Z_1 &= r_1 \cos \theta_o & ; & \quad X_1 = r_1 \sin \theta_o \\ Z_2 &= \frac{r_1}{2} \cos \theta_o - s_2 \sin \theta_o & ; & \quad X_2 = \frac{r_1}{2} \sin \theta_o + s_2 \cos \theta_o \end{aligned} \quad (79)$$

Inserting typical parameter values, H_{f_2} becomes [33]:

$$\frac{H_{f_2}}{E_J^0} = [-0.025 + 4.0 \delta_1 + 2.1 \delta_2] \sigma_z - [0.46 \delta_1 + 0.41 \delta_2] \sigma_x. \quad (80)$$

This completes step 1 of the demonstration.

To produce a TRP sweep, we must require (step 2) that

$$\begin{aligned} Z_0 - Z_1 \delta_1 - Z_2 \delta_2 &= at \\ X_1 \delta_1 + X_2 \delta_2 &= b \cos \phi_{trp}. \end{aligned} \quad (81)$$

Recalling that $t = (b/a)\tau$, and defining $Z_i = E_J^0 z_i$ and $X_i = E_J^0 x_i$, eq. (81) can be rewritten as

$$\begin{aligned} z_1 \delta_1 + z_2 \delta_2 &= z_0 - \left(\frac{b}{E_J^0} \right) \tau \\ x_1 \delta_1 + x_2 \delta_2 &= \left(\frac{b}{E_J^0} \right). \end{aligned}$$

Solving for δ_1 and δ_2 gives

$$\begin{aligned} \delta_1 &= \frac{x_2}{G} \left[\left(\frac{b}{E_J^0} \right) \tau - z_0 \right] + \frac{z_2}{G} \left(\frac{b}{E_J^0} \right) \cos \phi_{trp} \\ \delta_2 &= \frac{x_1}{G} \left[z_0 - \left(\frac{b}{E_J^0} \right) \tau \right] - \frac{z_1}{G} \left(\frac{b}{E_J^0} \right) \cos \phi_{trp}, \end{aligned} \quad (82)$$

where $G = x_1 z_2 - x_2 z_1$. Typical values for x_i and z_i for $i = 1, 2$ can be read off from eq. (80). Inserting these values into eq. (82) gives

$$\begin{aligned}\delta_1(\tau) &= 0.61 \left[z_0 - \left(\frac{b}{E_J^0} \right) \tau \right] - 3.1 \left(\frac{b}{E_J^0} \right) \cos \phi_{trp} \\ \delta_2(\tau) &= 0.68 \left[\left(\frac{b}{E_J^0} \right) \tau - z_0 \right] + 5.9 \left(\frac{b}{E_J^0} \right) \cos \phi_{trp}.\end{aligned}\quad (83)$$

Recall that a TRP sweep runs over times $-\tau_0/2 \leq \tau \leq \tau_0/2$, and that our simulations used $\tau_0/2 = 40, 60$. In Ref. [33], $\delta_1 \sim 10^{-3}$ and $\delta_2 \sim 10^{-4}$. To produce δ_1 and δ_2 of this size using eq. (83), we require that $b/E_J^0 \sim 10^{-4}$ and $z_0 \sim 10^{-4}$. With $E_J^0/\hbar = 100$ GHz, this requires $b/\hbar, Z_0/\hbar \sim 10$ MHz. The TRP sweep parameters a, B , and T_0 are then found from eq. (32) for given values of λ, η_4 , and τ_0 . Thus, with δ_1 and δ_2 given by eqs. (83), the persistent-current qubit Hamiltonian H_{f2} becomes

$$H_{f2} = -at \sigma_z - b \cos \phi_{trp} \sigma_x.$$

This completes step 2. In the rotating wave approximation (step 3), H_{f2} becomes

$$H_{f2} = -at \sigma_z - b \cos \phi_{trp} \sigma_x - b \sin \phi_{trp} \sigma_y \quad (84)$$

which is the Hamiltonian for a qubit subjected to a TRP sweep (eqs. (1) and (2)). We see that requiring the control fluxes $\delta_1(\tau)$ and $\delta_2(\tau)$ to satisfy eqs. (83) causes a TRP sweep to be applied to the persistent-current qubit. Unlike with the two previous SC qubit realizations, we see from eq. (81) that the inversion and twisting of the TRP control field $\mathbf{F}(t)$ is determined by linear combinations of the control fluxes δ_1 and δ_2 . In the case of the persistent-current qubit, we cannot (in general) attribute inversion to one control field and twisting to the other.

5 Discussion

In this paper we have presented simulation results which suggest that TRP sweeps should be capable of implementing a universal set of quantum gates \mathcal{G}_u that operate non-adiabatically and with high-fidelity. The one-qubit gates in \mathcal{G}_u were seen to operate with gate error probabilities satisfying $P_e < 10^{-4}$, and the two-qubit modified controlled-phase gate with $P_e < 1.27 \times 10^{-3}$. Using the rough-and-ready estimate for the accuracy threshold, $P_a \sim 10^{-4}$, we see that: (i) the TRP-generated one-qubit gates have error probabilities that fall below this threshold value; and (ii) the two-qubit gate comes within an order-of-magnitude of it. As was noted in Section 4, this high level of gate performance requires that the TRP sweep parameters be controllable to high precision. Finding a way to make TRP gates more robust is a major challenge that must be overcome if these sweeps are to become a viable means for universal control of a quantum computer. To that end, we are currently exploring the consequences of interlacing TRP sweeps with dynamical decoupling pulses [36, 37, 38] to produce an effective dynamics that preserves a group of symmetries G of the target gate U_t . By removing the part of the TRP dynamics that does not commute with G , it is hoped that the resulting effective dynamics will yield gate performance that varies more slowly with the sweep parameters, and makes it easier for the minimization algorithms to carry out their work.

TRP has been experimentally realized in NMR systems [15, 17], and these systems have allowed the controllable quantum interference effects that were predicted to arise from multiple passes through resonance per TRP sweep [16] to be observed [17]. A demonstration of how TRP sweeps can be applied to atomic systems using electric fields has also been given [18]. In this paper we have shown how TRP can be applied to both superconducting charge and flux qubits. In such superconducting qubit systems, a qubit is realized by a mesoscopic circuit and the control fields are gate voltages and highly localized magnetic fields that are applied directly to the circuit. These systems thus allow a TRP sweep to be applied to an individual qubit, unlike in NMR systems where the sweeps are applied to an ensemble of qubits. In the NMR setting, variation of the rf-magnetic field amplitude over the ensemble causes the largest problem for high precision control of the TRP sweep parameters [18]. Note that this difficulty does not arise with superconducting qubits. It would be interesting to work out an adaptation of the NMR experiment that observed the TRP quantum interference effects [17] to a superconducting qubit system. Since these interference effects are a direct consequence of the temporal phase coherence of the qubit wave function, the adapted experiment would provide a new, independent demonstration of quantum coherence in superconducting qubit systems. Such a translation of the NMR experiment is currently underway. Ref. [18] described a state tomography experiment that would test the TRP gate simulation results by measuring the output density matrix $\rho_{exp} = U_a|\psi_0\rangle\langle\psi_0|U_a^\dagger$ resulting from an initial state $|\psi_0\rangle$, for each of the TRP generated gates U_a presented in Section 3. Associated with each sweep is a target gate U_t and a corresponding target density matrix $\rho_t = U_t|\psi_0\rangle\langle\psi_0|U_t^\dagger$. Having measured ρ_{exp} , the gate fidelity could be calculated and compared with the fidelity obtained from the TRP gate simulations. There are now three possible physical systems where such an experiment could be carried out. For alternative applications of temporal phase coherence and rapid passage to quantum computing, see Refs. [39] and [40, 41], respectively.

Acknowledgements

M. Hoover was supported by the Illinois Louis Stokes Alliance for Minority Participation Bridge to the Doctorate Fellowship, and F. Gaitan thanks T. Howell III for continued support.

References

1. D. Aharonov and M. Ben-Or, *Fault-tolerant computation with constant error*, in Proceedings of the Twenty-Ninth ACM Symposium on the Theory of Computing, 176 (1997).
2. A. Y. Kitaev, *Quantum computation algorithms and error correction*, Russ. Math. Surv. **52**, 1191 (1997).
3. A. Y. Kitaev, *Quantum error correction with imperfect gates*, in Quantum Communication, Computing, and Measurement (Plenum Press, New York, 1997), pp. 181–188.
4. D. Gottesman, *Stabilizer codes and quantum error correction*, Ph. D. thesis, California Institute of Technology, Pasadena, CA (1997).
5. E. Knill, R. Laflamme, and W. H. Zurek, *Resilient quantum computation*, Science **279**, 342 (1998).
6. E. Knill, R. Laflamme, and W. H. Zurek, *Resilient quantum computation: error models and thresholds*, Proc. R. Soc. Lond. A **454**, 365 (1998).
7. J. Preskill, *Reliable quantum computers*, Proc. R. Soc. Lond. A **454**, 385 (1998).
8. F. Gaitan, *Quantum error correction and fault-tolerant quantum computing*, (CRC Press, Boca Raton, FL 2008),

9. D. Deutsch, *Quantum theory, the Church-Turing principle, and the universal quantum computer*, Proc. R. Soc. Lond. A **400**, 97 (1985).
10. D. Deutsch, *Quantum computational networks*, Proc. R. Soc. Lond. A **425**, 73 (1989).
11. A. Barenco, C. H. Bennett, R. Cleve, D. P. DiVincenzo, N. Margolus, P. Shor, T. Sleator, J. A. Smolin, and H. Weinfurter, *Elementary gates for quantum computation*, Phys. Rev. A **52**, 3457 (1995).
12. D. Deutsch, A. Barenco, and A. Ekert, *Universality in quantum computation*, Proc. R. Soc. Lond. A **449**, 669 (1995).
13. S. Lloyd, *Almost any quantum gate is universal*, Phys. Rev. Lett. **75**, 346 (1995).
14. P. O. Boykin, T. Mor, M. Pulver, V. Roychowdhury, F. Vatan, *On universal and fault-tolerant quantum computing*, in Proc. 40th Ann. Symp. on Found. Comp. Sc., 486 (1999).
15. J. W. Zwanziger, S. P. Rucker, and G. C. Chingas, *Measuring the geometric component of the transition probability in a two-level system*, Phys. Rev. A **43**, 3232 (1991).
16. F. Gaitan, *Temporal interferometry: A mechanism for controlling qubit transitions during twisted rapid passage with possible application to quantum computing*, Phys. Rev. A **68**, 052314 (2003).
17. J. W. Zwanziger, U. Werner-Zwanziger, and F. Gaitan, *Non-adiabatic rapid passage*, Chem. Phys. Lett. **375**, 429 (2003).
18. R. Li, M. Hoover, and F. Gaitan, *High fidelity single-qubit gates using non-adiabatic rapid passage*, Quant. Info. Comp., **7**, 594 (2007).
19. A. Abragam, *Principles of Nuclear Magnetism*, (Oxford University Press, New York 1961).
20. D. Suter, G. C. Chingas, R. A. Harris, and A. Pines, *Berry's phase in magnetic resonance*, Mol. Phys. **61**, 1327 (1987).
21. F. Gaitan, *Berry's phase in the presence of a non-adiabatic environment with an application to magnetic resonance*, J. Mag. Reson. **139**, 152 (1999), see eq. (14).
22. R. P. Feynman and A. R. Hibbs, *Quantum Mechanics and Path Integrals*, (McGraw-Hill, New York, 1965).
23. A. Shapere and F. Wilczek, *Geometric Phases in Physics*, (World Scientific, New Jersey, 1989).
24. W. H. Press, S. A. Teukolsky, W. T. Vetterling, and B. P. Flannery, *Numerical Recipes, 2nd ed.*, (Cambridge University Press, New York, 1992).
25. J. J. L. Morton, A. M. Tyryshkin, A. Ardavan, K. Porfyarakis, S. A. Lyon, and G. A. D. Briggs, *High fidelity single qubit operations using pulsed electron paramagnetic resonance*, Phys. Rev. Lett. **95**, 200501 (2005).
26. Y. Makhlin, G. Schön, and A. Shnirman, *Quantum-state engineering with Josephson-junction devices*, Rev. Mod. Phys. **73**, 357 (2001).
27. J. Q. You and F. Nori, *Superconducting circuits and quantum information*, Phys. Today **58**, No. 11, 42 (2005).
28. D. V. Averin, *Adiabatic quantum computation with Cooper pairs*, Solid State Commun. **105**, 659 (1998).
29. Y. Makhlin, G. Schön, and A. Shnirman, *Josephson junction qubits with controlled couplings*, Nature **386**, 305 (1999).
30. J. Q. You and F. Nori, *Quantum information processing with superconducting qubits in a microwave field*, Phys. Rev. B **68**, 064509 (2003).
31. P. W. Anderson, in *Lectures on the Many-Body Problem*, vol. 2, ed. E. R. Caianello (Academic Press, New York, 1964), p. 115.
32. M. F. Bocko, A. M. Herr, and M. J. Feldman, *Prospects for quantum coherent computation using superconducting electronics*, IEEE Trans. App. Superconductivity **7**, 3638 (1997).
33. T. P. Orlando, J. E. Mooij, L. Tian, C. H. van der Wal, L. S. Levitov, S. Lloyd, and J. J. Mazo, *Superconducting persistent-current qubit*, Phys. Rev. B **60**, 15398 (1999).
34. J. E. Mooij, T. P. Orlando, L. Levitov, L. Tian, C. H. van der Wal, and S. Lloyd, *Josephson persistent-current qubit*, Science **285**, 1036 (1999).
35. J. Q. You, X. Hu, S. Ashhab, and F. Nori, *Low-decoherence flux qubit*, Phys. Rev. B **75**, 140515(R) (2007).

36. L. Viola and S. Lloyd, *Dynamical suppression of decoherence in two-state systems*, Phys. Rev. A **58**, 2733 (1998).
37. P. Zanardi, *Symmetrizing evolutions*, Phys. Lett. A **258**, 77 (1999).
38. L. Viola, S. Lloyd, and E. Knill, *Universal control of decoupled quantum systems*, Phys. Rev. Lett. **83**, 4888 (1999).
39. S. Ashhab, J. R. Johansson, A. M. Zagoskin, and F. Nori, *Two-level systems driven by large-amplitude fields*, Phys. Rev. A **75**, 063414 (2007).
40. L. F. Wei, J. R. Johansson, L. X. Cen, S. Ashhab, and F. Nori, *Controllable coherent population transfers in superconducting qubits for quantum computing*, Phys. Rev. Lett., in press (2008).
41. C. Hicke, L. F. Santos, and M. I. Dykman, *Fault-tolerant Landau-Zener quantum gates*, Phys. Rev. A **73**, 012342 (2006).

Appendix A

Here we derive the dimensionless Hamiltonian $H_2(\tau)$ introduced in Section 2.2. It proves convenient to adopt the language of NMR, although a more general discussion is possible.

Consider a two-qubit system in which each qubit is Zeeman-coupled to an external magnetic field $\mathbf{B}(t)$, and the two qubits interact through the Ising interaction. As noted in Section 2.2, the Ising interaction was chosen because of its simplicity, and because it is present in many physical systems. It is a simple matter to alter the following arguments to include a different two-qubit interaction. Our starting point is thus the Hamiltonian

$$\frac{\overline{H}_2(t)}{\hbar} = -\frac{1}{2} \sum_{i=1}^2 \gamma_i \boldsymbol{\sigma}_i \cdot \mathbf{B}(t) - \frac{\pi}{2} J \sigma_{1z} \sigma_{2z}, \quad (\text{A.1})$$

where γ_i is the gyromagnetic ratio for qubit i , and J is the Ising interaction coupling constant. In the lab frame, $\mathbf{B}(t)$ has a static component $B_0 \hat{\mathbf{z}}$ and a time-varying component $2B_{rf} \cos \phi_{rf}(t) \hat{\mathbf{x}}$. In the rotating wave approximation $\mathbf{B}(t)$ reduces to

$$\mathbf{B}(t) = B_0 \hat{\mathbf{z}} + B_{rf} \cos \phi_{rf}(t) \hat{\mathbf{x}} - B_{rf} \sin \phi_{rf}(t) \hat{\mathbf{y}}. \quad (\text{A.2})$$

Introducing $\omega_i = \gamma_i B_0$ and $\omega_i^{rf} = \gamma_i B_{rf}$ ($i = 1, 2$), and inserting eq. (A.2) into eq. (A.1) gives

$$\frac{\overline{H}_2(t)}{\hbar} = \sum_{i=1}^2 \left[-\frac{\omega_i}{2} \sigma_{iz} - \frac{\omega_i^{rf}}{2} \{ \cos \phi_{rf} \sigma_{ix} - \sin \phi_{rf} \sigma_{iy} \} \right] - \frac{\pi}{2} J \sigma_{1z} \sigma_{2z}. \quad (\text{A.3})$$

Transformation to the detector frame is done via the unitary operator

$$U(t) = \exp [(i\phi_{det}(t)/2) (\sigma_{1z} + \sigma_{2z})].$$

The Hamiltonian in the detector frame is then [19]

$$\begin{aligned} \frac{\tilde{H}_2(t)}{\hbar} &= U^\dagger \left(\frac{\overline{H}_2(t)}{\hbar} \right) U - iU^\dagger \frac{dU}{dt} \\ &= \sum_{i=1}^2 \left[\left(-\frac{\omega_i}{2} + \dot{\phi}_{det} \right) \sigma_{iz} - \frac{\omega_i^{rf}}{2} \{ \cos(\phi_{det} - \phi_{rf}) \sigma_{ix} + \sin(\phi_{det} - \phi_{rf}) \sigma_{iy} \} \right] \\ &\quad - \frac{\pi}{2} J \sigma_{1z} \sigma_{2z}. \end{aligned} \quad (\text{A.4})$$

As explained in Section 2.1, to produce a TRP sweep in the detector frame it is necessary to sweep $\dot{\phi}_{det}$ and $\dot{\phi}_{rf}$ through a Larmor resonance frequency. We choose (somewhat arbitrarily) to sweep through the Larmor frequency ω_2 :

$$\begin{aligned}\dot{\phi}_{det} &= \omega_2 + \frac{2at}{\hbar} + \Delta \\ \dot{\phi}_{rf} &= \dot{\phi}_{det} - \dot{\phi}_4.\end{aligned}\tag{A.5}$$

Here $\phi_4(t) = (1/2)Bt^4$ is the twist profile for quartic TRP, and we have introduced a frequency shift parameter Δ whose value will be determined by the sweep parameter optimization procedure of Section 2.3. Inserting eqs. (A.5) into eq. (A.4), and introducing $\delta\omega = \omega_1 - \omega_2$ and $b_i = \hbar\omega_i^{rf}/2$ ($i = 1, 2$), we find

$$\begin{aligned}\frac{\tilde{\text{H}}_2(t)}{\hbar} &= \left[-\frac{(\delta\omega + \Delta)}{2} + \frac{at}{\hbar} \right] \sigma_{1z} - \frac{b_1}{\hbar} [\cos \phi_4 \sigma_{1x} + \sin \phi_4 \sigma_{1y}] \\ &\quad + \left[-\frac{\Delta}{2} + \frac{at}{\hbar} \right] \sigma_{2z} - \frac{b_2}{\hbar} [\cos \phi_4 \sigma_{2x} + \sin \phi_4 \sigma_{2y}] \\ &\quad - \frac{\pi}{2} J \sigma_{1z} \sigma_{2z}.\end{aligned}\tag{A.6}$$

We see that both qubits are acted on by a quartic TRP sweep in the detector frame. In keeping with our earlier choice of sweeping through the Larmor resonance of the second qubit, we use b_2 in the definitions of the dimensionless time τ , inversion rate λ , and twist strength η_4 :

$$\tau = \left(\frac{a}{b_2} \right) t\tag{A.7}$$

$$\lambda = \frac{\hbar a}{(b_2)^2}\tag{A.8}$$

$$\eta_4 = \left(\frac{\hbar B}{a^3} \right) (b_2)^2.\tag{A.9}$$

Since $\tilde{\text{H}}_2(t)/\hbar$ has units of inverse-time, and b_2/a has units of time (eq. (A.7)), multiplying eq. (A.6) by b_2/a and using eqs. (A.7)–(A.9) gives the dimensionless two-qubit Hamiltonian $\tilde{\text{H}}_2(\tau)$:

$$\begin{aligned}\tilde{\text{H}}_2(\tau) &= \left[-\frac{(d_1 + d_2)}{2} + \frac{\tau}{\lambda} \right] \sigma_{1z} - \frac{d_3}{\lambda} [\cos \phi_4 \sigma_{1x} + \sin \phi_4 \sigma_{1y}] \\ &\quad + \left[-\frac{d_2}{2} + \frac{\tau}{\lambda} \right] \sigma_{2z} - \frac{1}{\lambda} [\cos \phi_4 \sigma_{2x} + \sin \phi_4 \sigma_{2y}] \\ &\quad - \frac{\pi}{2} d_4 \sigma_{1z} \sigma_{2z},\end{aligned}\tag{A.10}$$

where

$$\begin{aligned}
d_1 &= \left(\frac{\delta\omega}{a}\right) b_2 \\
d_2 &= \left(\frac{\Delta}{a}\right) b_2 \\
d_3 &= \frac{b_1}{b_2} \\
d_4 &= \left(\frac{J}{a}\right) b_2.
\end{aligned} \tag{A.11}$$

As noted in Section 2.2, $\tilde{H}_2(\tau)$ has a degeneracy in the resonance frequency of the energy level pairs $(E_1 \leftrightarrow E_2)$ and $(E_3 \leftrightarrow E_4)$. To break this degeneracy we add the term

$$\Delta H = c_4 |E_4(\tau)\rangle\langle E_4(\tau)| \tag{A.12}$$

to $\tilde{H}_2(\tau)$, where $|E_4(\tau)\rangle$ is the instantaneous energy eigenstate of $\tilde{H}_2(\tau)$ with eigenvalue $E_4(\tau)$. Our final Hamiltonian is then

$$H_2(\tau) = \tilde{H}_2(\tau) + \Delta H \tag{A.13}$$

which is the Hamiltonian given in eq. (19). We see that $H_2(\tau)$ depends on the TRP sweep parameters (λ, η_4) , as well as on the parameters (d_1, \dots, d_4) and c_4 . From eq. (A.11) we see that d_1 , d_2 , d_3 , and d_4 are the dimensionless versions of, respectively, the Larmor frequency difference $\delta\omega = \omega_1 - \omega_2$, the frequency shift parameter Δ , the ratio $b_1/b_2 = \gamma_1/\gamma_2$, and the Ising coupling constant J .